Journal of Nanobiotechnology

RESEARCH

Open Access

Blocking copper transporter protein-dependent drug efflux with albumin-encapsulated Pt(IV) for synergistically enhanced chemo-immunotherapy

Man Fang[1,2†], Lei Cao[2,3,4,5†], Zhao Zhang[6], Zhen Yu[1,2], Yue Shen[1,2], Jieqi Chen[1,2], Juan Chen[1,2], Yue-Qin Li[2], Zhaoqian Liu[2,3,4], Yingcai Meng[1,2], Haihua Xiao[7], Qiang Qu[1,2*], Ji-Ye Yin[2,3,4,5*] and Xiang-Ping Li[1,2*]

Abstract

Non-small cell lung cancer (NSCLC) represents the most prevalent form of lung cancer, exerting a substantial impact on global health. Cisplatin-based chemotherapy is the standard treatment for NSCLC, but resistance and severe side effects present significant clinical challenges. Recently, novel tetravalent platinum compounds have attracted significant interest. While numerous studies concentrate on their functional modifications and targeted delivery, tumor-induced platinum resistance is frequently overlooked. Previous tetravalent platinum compound demonstrated antitumor activity, yet proved ineffective against cells exhibiting resistance to cisplatin. In order to enhance the efficacy and potential applications of tetravalent platinum in NSCLC, a glutathione (GSH)-responsive albumin nanoquadrivalent platinum (HSA@Pt) have been constructed. In light of previous research into drug conjugation, this study was to develop a combined chemo-immunotherapy approach. The HSA@Pt demonstrated high efficacy and low toxicity, with targeted tumor accumulation. Furthermore, Ammonium Tetrathiomolybdate (TM) has been demonstrated to exert a synergistic inhibitory effect on ATPase Copper Transporting Beta (ATP7B) and Programmed Death Ligand 1 (PD-L1), impede platinum efflux, induce cellular stress, and activate antitumor immunity. The findings suggest HSA@Pt's potential for clinical use and a novel chemo-immunotherapy strategy for NSCLC, enhancing the utility of established drugs through synergistic sensitization.

Keywords NSCLC, Novel tetravalent platinum, Albumin, Ammonium Tetrathiomolybdate, Tumor chemo-immunotherapy

†Man Fang and Lei Cao contributed equally to this work.

*Correspondence:
Qiang Qu
quqiang@csu.edu.cn
Ji-Ye Yin
yinjiye@csu.edu.cn
Xiang-Ping Li
xylxping@csu.edu.cn
[1]Department of Pharmacy, Xiangya Hospital, Central South University, Changsha 410008, Hunan, P. R. China
[2]National Clinical Research Center for Geriatric Disorders, Xiangya Hospital, Central South University, Changsha 410008, P. R. China
[3]Department of Clinical Pharmacology, Xiangya Hospital, Central South University, Changsha 410008, P. R. China
[4]Institute of Clinical Pharmacology, Hunan Key Laboratory of Pharmacogenetics, Central South University, Changsha 410008, P. R. China
[5]Engineering Research Center of Applied Technology of Pharmacogenomics, Ministry of Education, 110 Xiangya Road, Changsha 410008, P. R. China
[6]Central South University Xiangya Medical School, No. 172 Tongzipo Road, Yuelu District, Changsha 410013, P. R. China
[7]Beijing National Laboratory for Molecular Sciences, State Key Laboratory of Polymer Physics and Polymer Chemistry, Institute of Chemistry, Chinese Academy of Sciences, Beijing 100190, P. R. China

© The Author(s) 2025. **Open Access** This article is licensed under a Creative Commons Attribution-NonCommercial-NoDerivatives 4.0 International License, which permits any non-commercial use, sharing, distribution and reproduction in any medium or format, as long as you give appropriate credit to the original author(s) and the source, provide a link to the Creative Commons licence, and indicate if you modified the licensed material. You do not have permission under this licence to share adapted material derived from this article or parts of it. The images or other third party material in this article are included in the article's Creative Commons licence, unless indicated otherwise in a credit line to the material. If material is not included in the article's Creative Commons licence and your intended use is not permitted by statutory regulation or exceeds the permitted use, you will need to obtain permission directly from the copyright holder. To view a copy of this licence, visit http://creativecommons.org/licenses/by-nc-nd/4.0/.

Introduction

Lung cancer has one of the highest incidences and mortality rates worldwide. Among these, non-small cell lung cancer (NSCLC) represents the predominant form, exerting a profound impact on global cancer morbidity and mortality [1, 2]. Platinum drug, primarily cisplatin, is a pivotal component of first-line chemotherapy for NSCLC [3]. Nevertheless, a substantial number of clinical trials have demonstrated that the chemotherapeutic efficacy of cisplatin is inadequate, with over one-third of NSCLC patients exhibiting cisplatin resistance. Additionally, cisplatin has been associated with significant adverse effects, including nephrotoxicity, ototoxicity, and neurotoxicity [4, 5]. Clearly, the resistance and toxic side effects of cisplatin restrict its clinical application, and this issue requires urgent resolution.

To address the challenges posed by cisplatin resistance and toxicity, contemporary research is directed towards the engineering of a novel tetravalent platinum, which incorporates additional multifunctional groups through the axial moiety, thereby facilitating the objective of multi-target therapy or diagnostic and therapeutic integration [6–8]. This approach offers a promising avenue for resolving the challenges associated with the clinical application of cisplatin. It has been demonstrated that tetravalent platinum has superior antitumor effects compared to cisplatin. However, it remains ineffective in cisplatin-resistant tumors, a finding that was validated by our previous research [9, 10]. Similarly, the overall efficacy and toxicity of tetravalent platinum drugs (including omaplatin, isopropylplatin, and cytotoxic platinum) currently in clinical trials did not exceed that of cisplatin [11]. Therefore, focusing on the resistance mechanism of platinum drugs and seeking sensitisation strategies may further improve the efficacy and application prospect of tetravalent platinum.

Our previous studies were devoted to the field of platinum therapy in NSCLC [10, 12, 13]. We identified a number of genes and their variants that were associated with drug resistance or toxic side effects of platinum. These genes included *ATP7B* [14], *WISP1* [15], *ADCY1* [16] and *eIF3a* [13]. Among these, the *ATP7B rs9526814* variant has been demonstrated to enhance platinum resistance by influencing *ATP7B* gene expression. It may serve as a promising biomarker for predicting the sensitivity of NSCLC patients to cisplatin-based chemotherapy [14]. The ATP7B protein, as a P-ATPase, is crucial for maintaining copper homeostasis within cells, facilitating copper transport. Dysregulation of ATPases can result in Wilson disease, a condition characterised by disrupted copper metabolism [17–20]. ATP7B have also been demonstrated to facilitate the transport of platinum drugs and contribute to the development of resistance to cisplatin, carboplatin and oxaliplatin [21–23]. Studies have shown that targeting copper transport proteins such as ATP7A and ATP7B can significantly enhance the intracellular retention of platinum drugs by preventing their efflux [24, 25]. AmmoniumTetrathiomolybdate (TM), a copper chelator, is a commonly used clinical treatment for Wilson disease [26]. It has been demonstrated that TM is capable of binding to the metal-binding structural domains of ATPases, which inhibits cisplatin binding, maintains the effective concentration of cisplatin in tumor cells, and restores the sensitivity of tumor cells to platinum drugs [23]. Moreover, copper plays a pivotal role in regulating PD-L1 expression and promoting cancer immune escape, underscoring the potential for repurposing copper chelators as antitumor immune enhancers [27, 28]. Additionally, inhibitors like TM have been demonstrated to synergistically enhance the efficacy of cisplatin by disrupting copper-dependent pathways that regulate drug resistance and immune checkpoint proteins like PD-L1 [29]. Consequently, further investigation into the sensitising impact of TM on novel tetravalent platinum and its mechanism of action based on pharmacogenomics and immune may offer novel insights into the development, design and application of novel tetravalent platinum.

In order to further enhance the stability and targeting of tetravalent platinum drugs, researches have been conducted into the development of an array of drug delivery system [10, 12, 30]. Nanotechnology has demonstrated significant advantages in the therapeutic and diagnostic fields of pharmaceutics, including enhanced therapeutic efficacy, reduced adverse effects and multifunctional responsive release [31–34]. The human serum albumin (HSA)-based drug delivery system has long been the subject of considerable interest due to its biodegradability, non-immunogenic form and long half-life [35–37]. In light of the aforementioned findings, the present study employed HSA self-assembled with strongly hydrophobic Pt(IV) to form GSH-responsive nanoparticles (HSA@Pt) (Scheme 1A). The HSA@Pt was found to be highly efficacious and low-toxic, capable of targeted accumulation and retention at the tumor site. Further studies demonstrated that the release of Pt(IV) from HSA@Pt in response to the tumor microenvironment resulted in DNA damage and apoptosis through the reduction of platinum and the depletion of GSH. Concurrently, the objective was to enhance the efficacy of the platinum drugs by administering TM, which can enter tumor cells *via* free diffusion, and inhibiting the expression of copper transporter proteins ATP7B and PD-L1, and inhibit platinum efflux, which synergistically exacerbates the state of cellular stress and prompts the cells to release damage-associated molecular patterns and further activate the antitumor immune response (Scheme 1B). This study provides experimental evidence for albumin

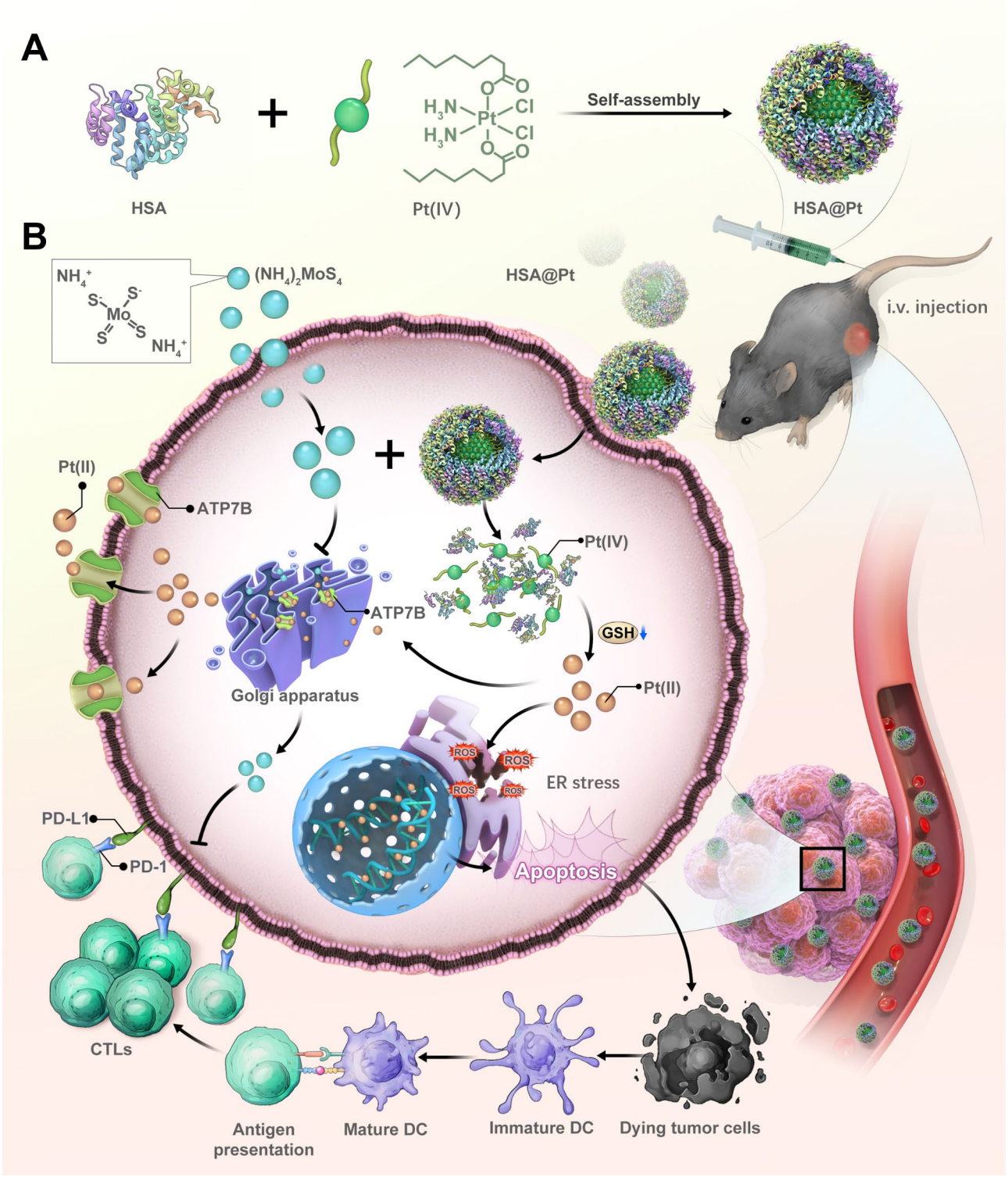

Sch. 1 Schematic illustration of HSA@Pt-based synergistic antitumor therapy *via* blocking platinum efflux and enhancing ER stress. (A) Chemical structure of Pt(IV), self-assembly of human serum albumin with Pt(IV) to form HSA@Pt. (B) Intravenously injected HSA@Pt preferred to accumulate and remain in tumor tissue through enhanced permeability and retention (EPR) effect. Stimulated by the tumor microenvironment, Pt(IV) released by HSA@Pt is reduced to divalent platinum by depleting GSH, causing DNA damage and inducing apoptosis. Concurrently, orally administered Ammonium Tetrathiomolybdate (TM) gains access to tumor cells *via* free diffusion, inhibits the expression of the copper transporter protein ATP7B as well as PD-L1, blocks platinum exocytosis, intensifies the cellular stress state, prompts the cells to release damage-associated molecular patterns, and further activates the antitumor immune response.

nanoplatinum as a drug with potential clinical application, and offers a new idea for chemotherapy of clinical NSCLC from the perspective of new use of old drugs and synergistic sensitisation.

Methods and materials

Materials and reagents

30% H_2O_2, L-Glutathione reduced (GSH) and n-Octanoic Anhydride ($(Me(CH_2)_6CO)_2O$) were purchased from Aladdin (Shanghai, China). Cisplatin (CisPt, purity: ≥ 99.99%) and Ammonium Tetrathiomolybdate (TM, purity: 99.97%) were purchased from Sigma (USA). All chemicals were obtained from commercial sources and used without further purification unless otherwise noted. RPMI-1640 medium, DMEM with 4.5 g/L glucose, penicillin/streptomycin (P/S), 0.25% trypsin-EDTA, and Fetal Bovine Serum (FBS) were purchased from Gibco (Gran Island, NY, U.S.A.). F12K medium was purchased from iCell (Shanghai, China). CCK8 assay kit, Actin-Tracker Green, ROS assay kit and ATP assay kit were purchase from Beyotime (Shanghai, China). Crystal Violet Ammonium Oxalate Solution, 1% and Red Blood Cell Lysis Buffer were purchase from Solarbio (Beijing, China). Live & dead viability/cytotoxicity assay kit was purchase from KeyGEN biotechnology (Nanjing, China). Annexin V-FITC/PI apoptosis kit was purchase from Elabscience Biotechnology (Wuhan, China).

Cell lines and animals

All cells were purchased from the American Type Culture Collection (ATCC, Manassas, VA, USA). C57BL/6 (female, 4–6 weeks old) were purchased from Hunan SJA Laboratory Animal Co., Ltd (Changsha, China) and raised in SPF animal rooms. All animal experiments were conducted in accordance with the guidelines of Hunan SJA Laboratory Institutional Animal Care and Use Committee (SJA2022128).

Cell culture

The mice lung carcinoma LLC cells were cultured in Dulbecco's modified Eagle's medium (4.5 g/L Liter Glucose) supplemented with 10% (V/V) fetal bovine serum, 100 μg/mL penicillin and 100 μg/mL streptomycin at 37 ℃ with 5% (V/V) CO_2. The human lung carcinoma A549 cells were cultured in RPMI 1640 supplemented with 10% (V/V) fetal bovine serum, 100 μg/mL penicillin and 100 μg/mL streptomycin at 37 ℃ with 5% (V/V) CO_2. The human lung carcinoma H1975, H1437, H827, H23, H1299 and A549DDP cells were cultured in RPMI 1640 supplemented with 10% (V/V) fetal bovine serum, 100 μg/mL penicillin and 100 μg/mL streptomycin at 37 ℃ with 5% (V/V) CO_2. When the degree of cell fusion reached 80%, the cells were digested with 0.25% trypsin-EDTA, and then sub-cultured or inoculated in cell plates for subsequent experiments.

Preparation and characterization of HSA@Pt

Furthermore, 50 μL of a 10 mg mL^{-1} Pt(IV) prodrug solution was added to 3 mL of a 3 mg mL^{-1} HSA solution, which was then subjected to magnetic stirring to facilitate self-assembly, resulting in the production of HSA@Pt. The Pt concentration in HSA@Pt was subsequently determined by ICP-MS. Subsequently, the hydrodynamic size of HSA@Pt was determined by dynamic light scattering. Finally, after negative staining with phosphotungstic acid, the morphology and shape of HSA@Pt were observed by transmission electron microscopy (TEM).

Pt released from HSA@Pt

5 mL of HSA@Pt at a Pt concentration of 100 μM was transferred to a pre-swelled dialysis bag (MWCO: 3500 Da), which was then immersed into 200 mL PBS or aqueous glutathione solution (200 mL, 10 mM GSH) in a shaking culture incubator at 37 °C. At different time points (0, 1, 2, 4, 6, 10, 12, 24, 48 h), 1 mL of sample solution was taken from the dialysate. The corresponding fresh solution (1 mL) was immediately added to the dialysate. All samples were subjected to analysis by ICP-MS. The Pt released from the micelles was expressed as a percentage of the cumulative Pt in the dialysate relative to the total Pt in the nanoparticles.

Intracellular Pt content

A549 cells were treated with PBS, TM, CisPt, Pt(IV), and HSA@Pt (10 μM Pt), or a combination with TM (100 μM) for 24 h. Following the removal of cellular debris through a PBS wash, cell samples were obtained. The collected cell samples were transferred to the bottom of the PTFE digestion cup, and 10 mL of a nitric acid-perchloric acid mixed solution (9:1) was added. The cup was then placed on a hot plate for digestion until the digested solution exhibited a light yellow or colorless appearance. The digestion solution should then be transferred into a 2-mL centrifuge tube and washed with nitric acid solution on several occasions. It should then be combined with a volumetric flask and the appropriate volume of nitric acid solution added, before being mixed thoroughly. The intracellular platinum content was quantified by ICP-MS.

Intracellular ROS generation

H_2DCF-DA assay was applied to evaluate the intracellular ROS levels. Firstly, A549 cells were treated with PBS, TM, CisPt, Pt(IV), and HSA@Pt (10 μM Pt), or a combination with TM (100 μM) for 24 h. Following this, the cells were incubated with H_2DCF-DA for 30 min, washed twice with PBS, and stained with DAPI for 10 min. The

fluorescence images were analyzed by CLSM, and ROS production was quantified by FCM.

Cell viability assays

A549, H1299, LLC and A549DDP cell lines were seeded in 96-well plates at a density of 8×10^3 cells per well and cultured for 48 h. The cells were subsequently treated with PBS, TM, CisPt, Pt(IV), and HSA@Pt (10 μM Pt), or a combination with TM (100 μM) for 24 h. The viability of the cells was evaluated through the incubation of the samples with 10% CCK8 for 30 min, followed by the measurement of the absorbance at 450 nm *via* Bio-Tek.

Apoptosis analysis

Cellular apoptosis was assessed with an Annexin V-FITC apoptosis detection kit according to the manufacturer's instructions. Briefly, 3×10^5 A549 cells were seeded in 12-well plates. After a 12-hour incubation period, the cells were treated with PBS, TM, CisPt, Pt(IV), and HSA@Pt (10 μM Pt), or a combination with TM (100 μM) for 24 h. Following this, the cells were washed with PBS and incubated with Annexin/PI reagent for 15 min at 37 ℃ in the dark. Subsequently, the cells were immediately analyzed by FCM.

Colony formation assays

A549 cells were seeded onto 6-well plates at a density of 800 cells per well and cultured for 12 h. Following this, the cells were treated with PBS, TM, CisPt, Pt(IV), and HSA@Pt (10 μM Pt), or a combination with TM (100 μM) for 24 h. The following day, the culture medium was replaced with fresh medium, which was subsequently changed every week. Finally, after removing the supernatant, the colonies were washed with PBS, fixed with 4% paraformaldehyde for 20 min, stained with 1% crystal violet for 10 min, and then photographed.

Western blot analysis

A549 cells were treated with PBS, TM, CisPt, Pt(IV), and HSA@Pt (10 μM Pt), or a combination with TM (100 μM). Incubation for 24 h, RIPA lysis buffer (P0013B, Beyotime) was then added to the cells, followed by the extraction of proteins *via* centrifugation at a speed of 12,000 rpm for 15 min. The protein concentration was determined with the BCA protein assay kit (P0011, Beyotime). Afterward, an equivalent amount of proteins were separated on a 10% SDS-PAGE and transferred onto the PVDF membrane by a gel-electrophoretic apparatus (Bio-Rad mini, USA). The membrane was blocked in TBS-T solution with 5% skim milk for 1 h. The membrane was incubated with primary antibodies against PD-L1 (ab205921, Abcam), C-Caspase 3 (ab32042, Abcam), Bcl-2(ab182858, Abcam), Bax (ab182733, Abcam), Tubulin (ab7291, Abcam) and β-actin (ab6276, Abcam) overnight at 4 °C. Then, the PVDF films were washed 3 times for 30 min and incubated with HRP-conjugated antibodies (A0208, Beyotime) for 2 h at room temperature. The Western blot images were captured using a Gel imaging system (Amersham ImageQuant 800, Cytiva) with 200 μL of ECL chemiluminescent reagent (KF001, Affinity) added on top of the membrane. Tubulin and β-actin were used as the protein loading control.

Measurement of cell surface PD-L1

The FCM method was employed for the purpose of detecting the presence of PD-L1 on the surface of the cells. A549 cells were seeded in a 12-well plate at a density of 3×10^5 cells / well. Then, the cells were treated with PBS, TM, CisPt, Pt(IV), and HSA@Pt (10 μM Pt), or a combination with TM (100 μM) for 24 h. The cells were collected and treated with 1% BSA for blocking. Subsequently, PD-L1 primary antibody (ab205921, Abcam) was added and after 3 washes with PBS, Alexa Fluor 488-conjugated secondary antibody was applied to the cells, which were then analyzed by FCM.

Measurement of ATP7B expression

For CLSM analysis of ATP7B expression, A549 cells were seeded on a live cell imaging glass bottom dish with a density of 1×10^5 cells/well. Subsequently, the cells were treated with PBS, TM, CisPt, Pt(IV), and HSA@Pt (10 μM Pt), or a combination with TM (100 μM). After incubating for 24 h, the cells were washed with PBS and fixed with 100% methanol for 5 min at room temperature. Subsequently, the cells were washed again with PBS and permeabilized with 0.1% Triton X-100 for 5 min. Following a 20-minute blockage with 1% BSA, the cells were then incubated overnight with ATP7B primary antibody (#AF0410, Affinity; ab124973, Abcam) diluted in blocking buffer. The next day, the cells were washed three times with PBS and incubated with Alexa Fluor 488-conjugated secondary antibody for 3 h. Finally, nuclear DNA was labeled blue with DAPI and images were captured with a confocal microscope.

BMDCs mature in vitro

Bone marrow-derived dendritic cells (BMDCs) were generated from female C57BL/6 mice aged 4–6 weeks. The cells were cultured in RPMI 1640 medium supplemented with 10% FBS, GM-CSF (20 ng mL^{-1}, Beyotime), and interleukin-4 (IL-4) (10 ng mL^{-1}, Beyotime) at 37 °C with 5% (V/V) CO_2. Following a five-day incubation period, the pretreated LLC cells were co-incubated with the BMDCs for a further 24 h. Thereafter, the DCs were stained with the corresponding antibodies (anti-mouse CD11c-PE, anti-mouse CD80-FITC, anti-mouse CD86-APC, Biolegend, USA) prepared in 0.1% BSA in PBS for

1 h at room temperature. The cells were finally analyzed by FCM.

Metabolomics

A549 cells cultured in 6-well plates (triplicates) were subjected to different treatments (PBS, TM, CisPt, HSA@Pt+TM (10 μM Pt, 100 μM TM)) for 24 h, which were next washed with 1x PBS twice before being extracted with 500 μL ice-cold extraction solvent (water: methanol: chloroform = 100:180:120, v/v/v). After shaking well for 1 min, 150 μL water was then added into the Eppendorf tube and centrifuged at 1000 g for 15 min at 4 °C. 400 μL supernatant was transferred to liquid chromatography vials, spun dry, and reconstituted to 40 μL for metabolomic analysis. All metabolites were detected by UPLC (Ultimate 3000, Thermo Fisher Scientific, San Jose, CA, USA)-ESI-Qrbitrap-MS (Orbitrap Fusion Lumos, Thermo Fisher Scientific, San Jose, CA, USA). Identification and relative quantification of the data were conducted by Compound discoverer (3.1). The follow-up statistical and enrichment analysis of metabolomic and lipidomic was based on MetaboAnalyst 6.0 (https://www.metaboanalyst.ca/).

Biodistribution of HSA@Pt in vivo

Female C57BL/6 mice were purchased from Hunan SJA Laboratory Animal Co., Ltd (Changsha, China) and raised in SPF animal rooms. Mice received a subcutaneous injection of 5×10^6 LLC cells at the right flank to build an LLC solid tumor-bearing mouse model. The mice were intravenously injected with HSA@Cy7.5 when the tumor volume reached approximately 200 mm^3. Imaging was conducted with an IVIS Spectrum (PerkinElmer, USA) at 1 h, 4 h, 7 h, 12 h, 24 h, 30 h, 36 h, and 48 h post-injection, respectively (excitation wavelength: 745 nm, fluorescence emission signal wavelength: 840 nm). At 48 h post-injection, the mice were sacrificed, and tumors and major organs were collected for ex vivo imaging.

In vivo antitumor efficacy evaluation

LLC tumor-bearing mice were randomly divided into 6 groups followed by intravenous injection with Saline, TM, CisPt and HSA@Pt (2.5 mg/kg Pt), or a combination with TM (0.5 mg/kg) on days 0, 3, 6, 9, 12, respectively. The tumor volume and mouse weight of each group was measured every three days, and the tumor volume (mm^3) was calculated as $V = (a \times b^2) / 2$, where a and b are the length and width of the tumor, respectively.

Immunohistochemical and Immunofluorescence analyses

The solid tumor were harvested from LLC tumor-bearing mice on the 18th day of tumor inoculation for histological observation by standard H&E staining, immunohistochemical and immunofluorescence staining. For H&E staining, the excised tumor and organs were fixed in 4% paraformaldehyde solution, embedded in paraffin, sectioned, and stained with hematoxylin and eosin (H&E). The sections were then observed under a fluorescence microscope (IX83, Olympus). Additionally, the expression of ATP7B in the tumor tissues were further determined through immunohistochemistry analysis, according to the manufacturer's instructions: ATP7B (#AF0410, Affinity). For detecting the expression of PD-L1 and infiltration of $CD8^+$ T cells in tumor tissues, frozen tumor sections were fixed, and blocked with 1% BSA. Then the sections were incubated with primary antibodies against PD-L1 (ab205921, Abcam) and CD8 (ab217344, Abcam) overnight at 4 ℃, followed by processing with corresponding second antibodies. Nuclei were counterstained with DAPI (ab228549, Abcam) and then the stained sections were imaged with a confocal laser scanning microscope.

Flow cytometric analysis of tumor immune microenvironment

Fresh tumors, spleen, and draining lymph node tissue were collected for antitumor immune response analysis via FACS. Samples were briefly dissociated into single-cell suspensions, followed by removal of red blood cells by red blood cell lysis buffer (Solabio). Subsequently, the samples were blocked with 0.1% BSA in PBS and incubated with relevant antibodies at room temperature for 1 h. To characterize T cells, TAM in the tumor, the cells underwent staining with anti-mouse CD3-PE, anti-mouse CD4-APC, anti-mouse CD8-FITC, anti-mouse F4/80-PE, anti-mouse CD80-FITC, and anti-mouse CD206-APC (Biolegend, USA). To analyze T cells in spleen, cells were stained with anti-mouse CD3-PE, anti-mouse CD4-APC, anti-mouse CD8-FITC (Biolegend, USA). For the analysis of memory T cells in spleen cells were stained with anti-mouse CD3-PE, anti-mouse CD8-FITC, CD44-PC5.5, and anti-mouse CD62L-APC (Biolegend, USA). For the analysis of DCs in tumors and lymph nodes, cells were stained with anti-mouse CD11c-PE, anti-mouse CD80-FITC, and anti-mouse CD86-APC (Biolegend, USA). Flow cytometric data acquisition was performed with CytExpert software, and the data were processed with FlowJo software. For ease of reference, the gating strategies are shown in Figure S17-22.

Statistical analysis

All statistical analysis and statistical graph generation were performed using GraphPad Prism 8. Unless otherwise stated in the figure legend, data are presented as mean ± SD of at least 3 independent experiments of biological replicates. Statistical significance was analyzed using one-way ANOVA or two-way ANOVA test with Tukey's multiple comparisons test. *P* values less than

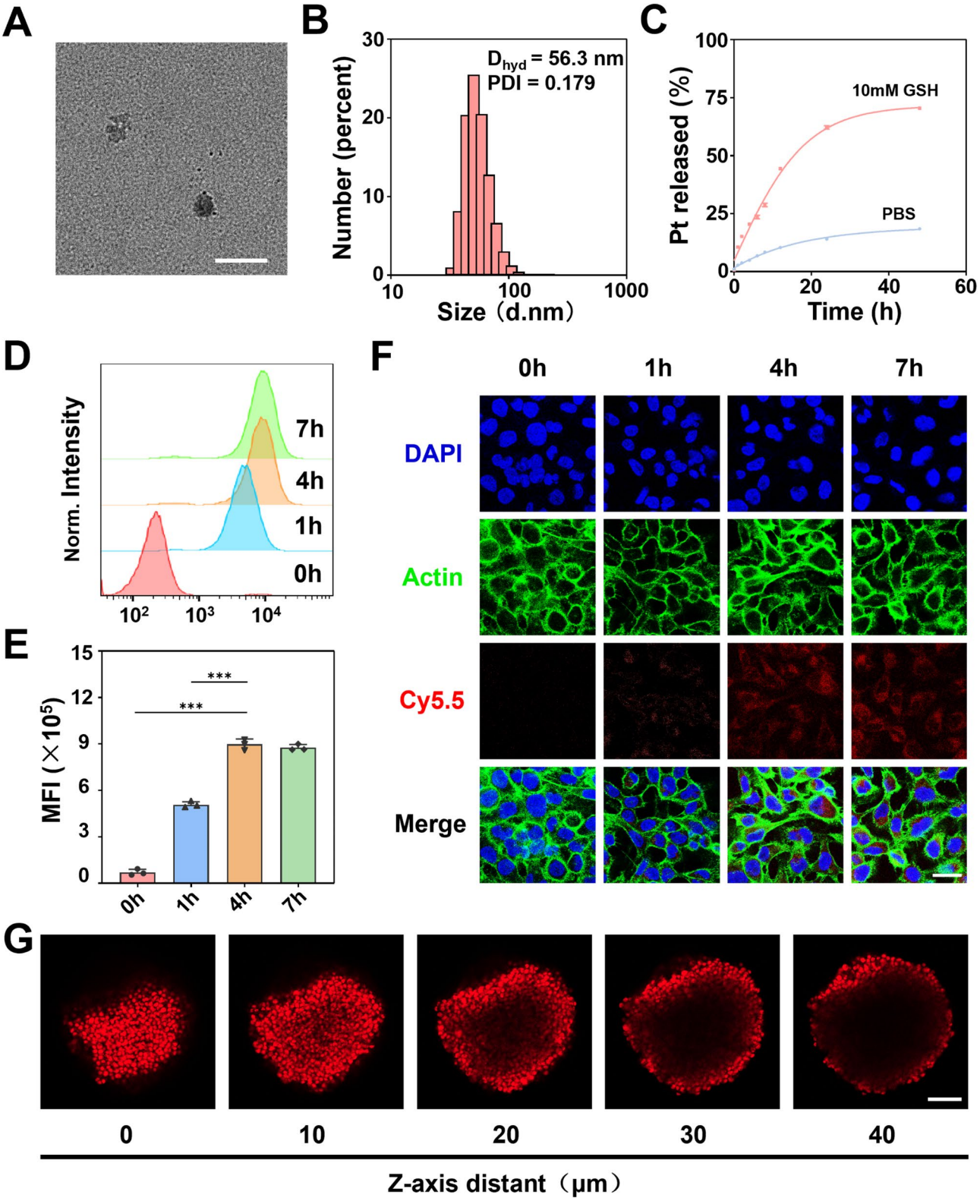

Fig. 2 (See legend on next page.)

(See figure on previous page.)

Fig. 1 Preparation and characterization of HSA@Pt. (A) TEM images of HSA@Pt. Scalar bar: 100 nm. (B) Hydrodynamic diameters of HSA@Pt measured by DLS. (C) Cumulative release of Pt from HSA@Pt in the presence of 10 mM GSH or PBS at 37 ℃, respectively. (D) Flow cytometric profiles and (E) the corresponding quantification of intracellular uptake of HSA@Cy5.5 for 0 h, 1 h, 4 h and 7 h, respectively, in A549 cells. (F) CLAS images of A549 cells treated with Cy5.5-labeled HSA@Pt at 0 h, 1 h, 4 h and 7 h, respectively. Scalar bar: 50 μm. (G) The confocal images of Cy5.5-labeled HSA@Pt endocytosed by H1299 3D spheroids. Scalar bar: 100 μm. Cell nuclear is strained by DAPI with blue fluorescence. The red fluorescence and green fluorescence come from Cy5.5 and cell skeleton stained with Actin, respectively. $n = 3$. Data are presented as mean ± SD. Statistical significances between every two groups were calculated *vivo* one-way ANOVA with Tukey's multiple comparisons test. *$p < 0.05$, ** $p < 0.01$, *** $p < 0.001$.

0.05 were considered statistically significant (*$p < 0.05$, **$p < 0.01$, ***$p < 0.001$).

Results and discussion

ATP7B expression correlating with the platinum-resistant of NSCLC

To obtain Pt(IV), cisplatin was initially subjected to an oxidative modification, which resulted in the formation of a Pt(IV) precursor. Subsequently, n-octanoic anhydride was reacted with the aforementioned Pt(IV) precursor, leading to the formation of Pt(IV) (Scheme S1, Figures S1 and S2). Previous studies have demonstrated that Pt(IV) exhibits potent antitumor activity in vitro [10]. However, in the context of cisplatin-resistant cell lines, the antitumor activity of Pt(IV) did not exceed that of cisplatin (Figure S3A-3D).

Previous studies have demonstrated that the *ATP7B rs9526814* variant is associated with platinum resistance by influencing *ATP7B* gene expression. This could represent a potential biomarker for predicting the sensitivity to cisplatin-based chemotherapy in NSCLC patients [14]. Consequently, the present study concentrated on ATP7B, while other mechanisms leading to platinum resistance or immune escape in NSCLC were not explored. In order to validate the relationship between the high expression of ATP7B and the cellular resistance to cisplatin, the study examined the expression of ATP7B in different cell lines by protein blotting. The results demonstrated that the expression of ATP7B was markedly elevated in the A549DDP cells line in comparison to A549 cells (Figure S4). The findings indicate that resistance to Pt(IV) may be attributable to elevate ATP7B expression. It may therefore be posited that a novel combination strategy targeting ATP7B may prove an efficacious approach to the treatment of NSCLC with novel Pt(IV).

In order to investigate the impact of TM on the expression of the ATP7B protein at the cellular level, the present study was supplemented with the following experiments for demonstration purposes. Firstly, A549DDP cells was treated with different concentrations (0, 20, 50 and 100 μM) of TM for 24 h. Thereafter, the intracellular expression of ATP7B was examined by Western blot (Figure S5A), flow cytometry (Figure S5B and S5C), and immunofluorescence (Figure S5D), respectively. The results demonstrated that TM induced the down-regulation of ATP7B protein in A549DDP cells in a dose-dependent manner. Consequently, it can be concluded that TM can affect ATP7B expression at the protein level.

Preparation and characterization of HSA@Pt

To enhance the stability and targeting of Pt(IV), the study employed a human serum albumin solution with Pt(IV) that was prepared into nanoparticles and labelled as HSA@Pt through self-assembly. The encapsulation and drug loading rates of platinum in HSA@Pt were 56.4 ± 1.6% and 15.4 ± 3.2%, respectively, as determined by ICP-MS. Transmission electron microscopy (TEM) revealed that the particle size of HSA@Pt was approximately 50 nm and exhibited a uniform and complete spherical shape (Fig. 1A). Furthermore, dynamic light scattering (DLS) revealed an average particle size of HSA@Pt to be approximately 56.3 nm with a polydispersity index (PDI) of 0.179 (Fig. 1B). Furthermore, the particle size of HSA@Pt in a 10% FBS 1640 complete medium and saline were observed to remain relatively stable over a period of 7 and 29, with an average size of approximately 55 nm and 60 nm, respectively (Figure S6). Subsequently, the cumulative release rate of HSA@Pt under different conditions (PBS, 10 mM GSH) of the platinum drug was investigated. The results demonstrated that the release rate of the platinum drug from HSA@Pt in PBS was only 18.51% within 48 h. The release rate of the platinum drug from HSA@Pt was significantly higher in the presence of GSH. After 48 h, the released platinum reached 70.49% in the presence of 10 mM GSH, which was 3.81 times higher than the release rate in PBS with the same treatment time. This fully demonstrated the reduction-sensitive responsive release property of HSA@Pt (Fig. 1C).

Subsequently, in order to quantify the cellular uptake of HSA@Pt, the study proceeded to label HSA@Pt (HSA@Cy5.5) with Cy5.5 (red) and to treat A549 cells for varying durations (0 h, 1 h, 4 h, 7 h) with the nanoparticles. The results of flow cytometry demonstrated that the fluorescence intensity in A549 cells was enhanced with the increase of treatment time. Specifically, the fluorescence intensity in cells after 7 h of treatment was approximately 1.73 times higher than that in cells after 1 h of treatment (Fig. 1D and E). To visualise the process of cellular uptake, the study employed confocal laser microscopy (CLSM), which revealed a gradual enhancement in intracellular red fluorescence intensity with increasing treatment time (Fig. 1F). Furthermore, the study constructed

3D tumor cell spheres to observe the capacity of HSA@Cy5.5 to penetrate these structures. It was observed that the red fluorescence intensity decreased from the periphery to the inner layer of the 3D tumor sphere as the depth increased from 0.0 μm to 40.0 μm. This indicated that the uptake of HSA@Pt by tumor cells decreased with increasing depth (Fig. 1G). In conclusion, tumor cells can rapidly internalise HSA@Pt within a relatively short timeframe.

In vitro anticancer effects of HSA@Pt combined with TM

In order to validate the synergistic effect of TM in combination with platinum, studies were conducted on A549 cells. A549 cells were treated with different platinum drugs or combined with TM, and the intracellular platinum concentration under different drug treatments was quantified by ICP-MS. The results demonstrated that the intracellular platinum concentration in HSA@Pt-treated cells was markedly elevated in comparison to cisplatin and Pt(IV) treatments, exhibiting a 2.40-fold and 1.83-fold increase, respectively. In particular, the intracellular platinum concentration within the HSA@Pt-treated cells was increased by 11.27-fold in combination with TM (Fig. 2A). The accumulation of platinum in tumor cells has been observed to induce cellular stress and apoptosis. In order to detect the stress state of cells, the study employed immunofluorescence and flow cytometry experiments utilising the DCFH-DA fluorescent probe to assess ROS levels in A549 cells treated with different drugs. The flow cytometry results demonstrated that the highest fluorescence intensity was observed in HSA@Pt+TM-treated cells, which exhibited a 1.29-fold and a 1.13-fold increase in fluorescence intensity compared to HSA@Pt- and Pt(IV)+TM-treated cells, respectively (Fig. 2B and C). The confocal microscopy results demonstrated that the intensity of green fluorescence in cells treated with HSA@Pt+TM was markedly higher than that observed in cells treated with HSA@Pt versus Pt(IV)+TM (Fig. 2D). The aforementioned results indicated that the accumulation of platinum was elevated in Pt(IV) versus HSA@Pt-treated tumor cells in comparison with cisplatin. Furthermore, TM was observed to significantly elevate intracellular platinum accumulation, which in turn induced a strong oxidative stress in the cells.

In order to test the in vitro toxicity of HSA@Pt, the study was conducted in different lung cancer tumor cell lines, including A549, H1299, LLC, and A549DDP. The cytotoxicity of HSA@Pt was then subjected to a CCK8 assay. The results demonstrated that the IC50 of CisPt in the A549 cell line was 10.46 μM, while the IC50 of HSA@Pt was 0.63 μM, which is equivalent to 1/16 of that of CisPt. This variability was particularly evident in the drug-resistant cell lines. In the drug-resistant strain A549DDP, the IC50 of CisPt was 34.76 μM, whereas that of HSA@Pt in the same strain was 1.45 μM, representing a 24-fold difference. The results showed that compared with traditional CisPt, HSA@Pt had significantly lower IC50 for NSCLC cells with different genetic backgrounds (Figure S7). Overall, the antitumor effect of HSA@Pt was found to be significantly elevated in comparison to CisPt, irrespective of the lung cancer cell line. Secondly, the experiment analysed the apoptosis under different treatments by means of Annexin V-FITC and propidium iodide (PI) double staining in the A549 cell line. The results demonstrated that the apoptosis rate of HSA@Pt-treated cells, which reached 29.70%, was 2.79 times higher than that of CisPt-treated cells (10.66%) (Fig. 2E and S8). Subsequently, a clone formation assay was employed to examine the long-term impact of diverse pharmacological interventions on the proliferation of A549 cells. The results demonstrated that, in comparison to the control group, both the HSA@Pt and HSA@Pt+TM treatments exhibited a pronounced inhibitory effect on the clone formation of A549 cells (Fig. 2F). Finally, the distribution of live and dead cells was observed by live-dead staining of A549 2D cells with H1299 3D cell spheres. It was also found that the number of dead cells (red color) was significantly higher after HSA@Pt treatment than that of control-treated cells (Fig. 2G and S9). In summary, in vitro, HSA@Pt+TM has more efficient antitumor activity.

Blocked platinum efflux and enhanced ER stress by HSA@Pt combined with TM in vitro

Cisplatin-based chemotherapeutic agents have the capacity to cross-link with DNA following their entry into tumor cells. This results in the damage of DNA, the regulation of the expression of Bax and Bcl-2, the activation of the mitochondrial apoptotic pathway and the activation of Caspase 3 following the release of cytochrome c into the extracellular space [38, 39]. This ultimately contributes to the occurrence of apoptosis. To ascertain the extent of apoptosis induced by HSA@Pt in tumor cells, the study initially employed the protein blotting (WB) method to analyse the expression of apoptosis-related proteins in A549 cells treated with different drugs. The results demonstrated that, in comparison to the control group, HSA@Pt markedly enhanced the up-regulation of Bax and Cleaved-caspase 3, while concurrently reducing the expression of Bcl-2 (Fig. 3A, B and S10). To verify the synergistic effect between TM and CisPt, the study detected the expression level of the ATP7B protein in A549 cells treated with different drugs by immunofluorescence. The results demonstrated that the intensity of red fluorescence was markedly diminished in cells treated with a combination of TM and HSA@Pt compared to those treated with a single drug (Fig. 3C). Consequently, the co-administration of TM and HSA@Pt could enhance the intracellular platinum concentration in tumor cells by

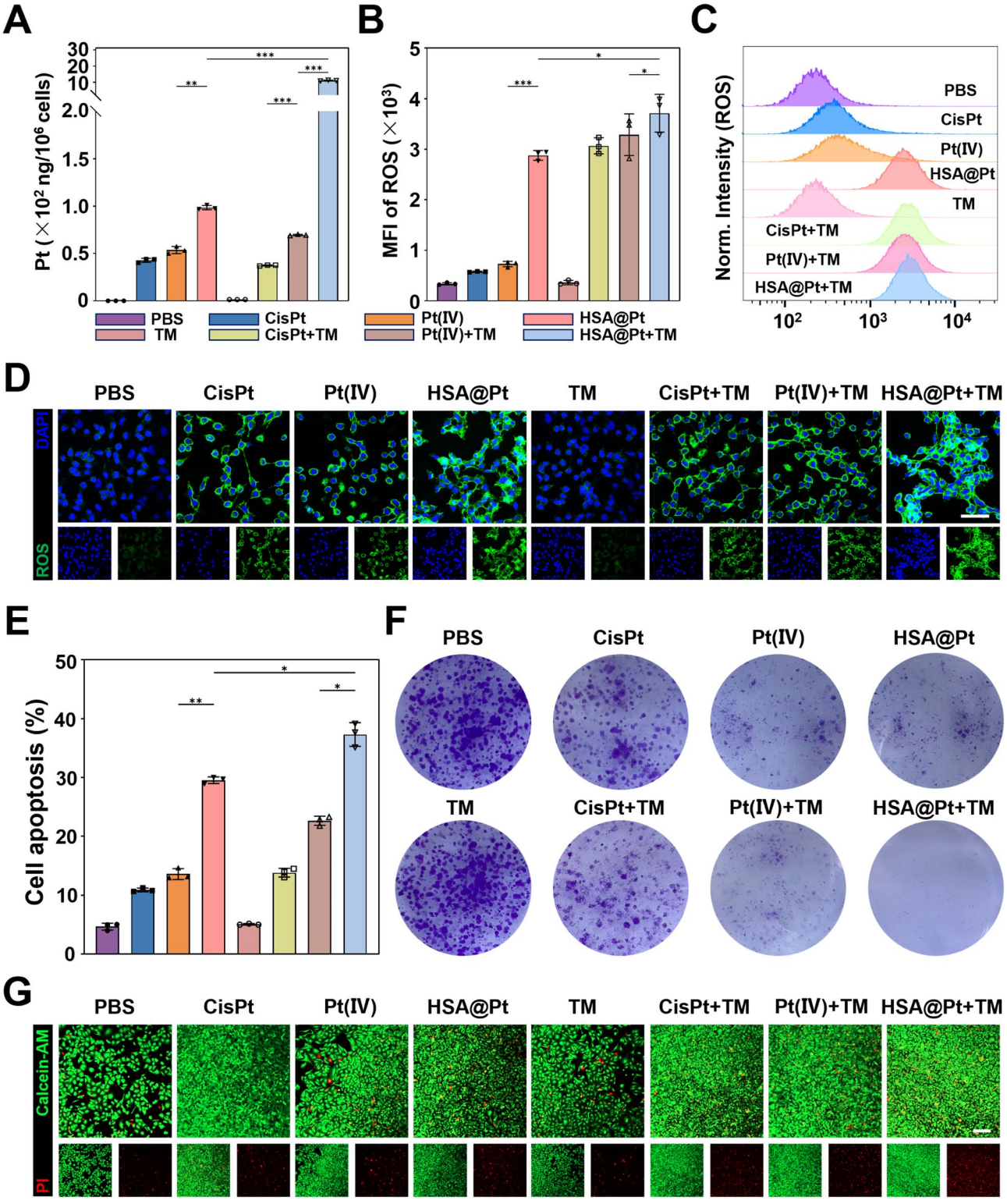

Fig. 2 In vitro anticancer effects of HSA@Pt combined with TM. (A) Amount of accumulated Pt in A549 cells treated with PBS, TM, CisPt, Pt(IV) and HSA@Pt (10 μM Pt), or combination with TM (100 μM) for 24 h, respectively. (B) ROS generation in A549 cells after various treatments by flow cytometry (C) and the corresponding quantification of ROS generation. (D) Intracellular ROS generation in A549 cells after various treatments by CLSM. Scale bar: 100 μm. (E) Quantification of apoptotic ratio *via* FCM in A549 cells with various treatments. (F) Final colonies stained with crystal violet dye after different treatments for two weeks. (G) The 2D CLSM images of A549 cells stained with calcein-AM (green, viable) and PI (red, dead) after various treatments. Scale bar: 200 μm. $n = 3$. Data are presented as mean ± SD. Statistical significances between every two groups were calculated *via* one-way ANOVA with Tukey's multiple comparisons test. *$p < 0.05$, ** $p < 0.01$, *** $p < 0.001$.

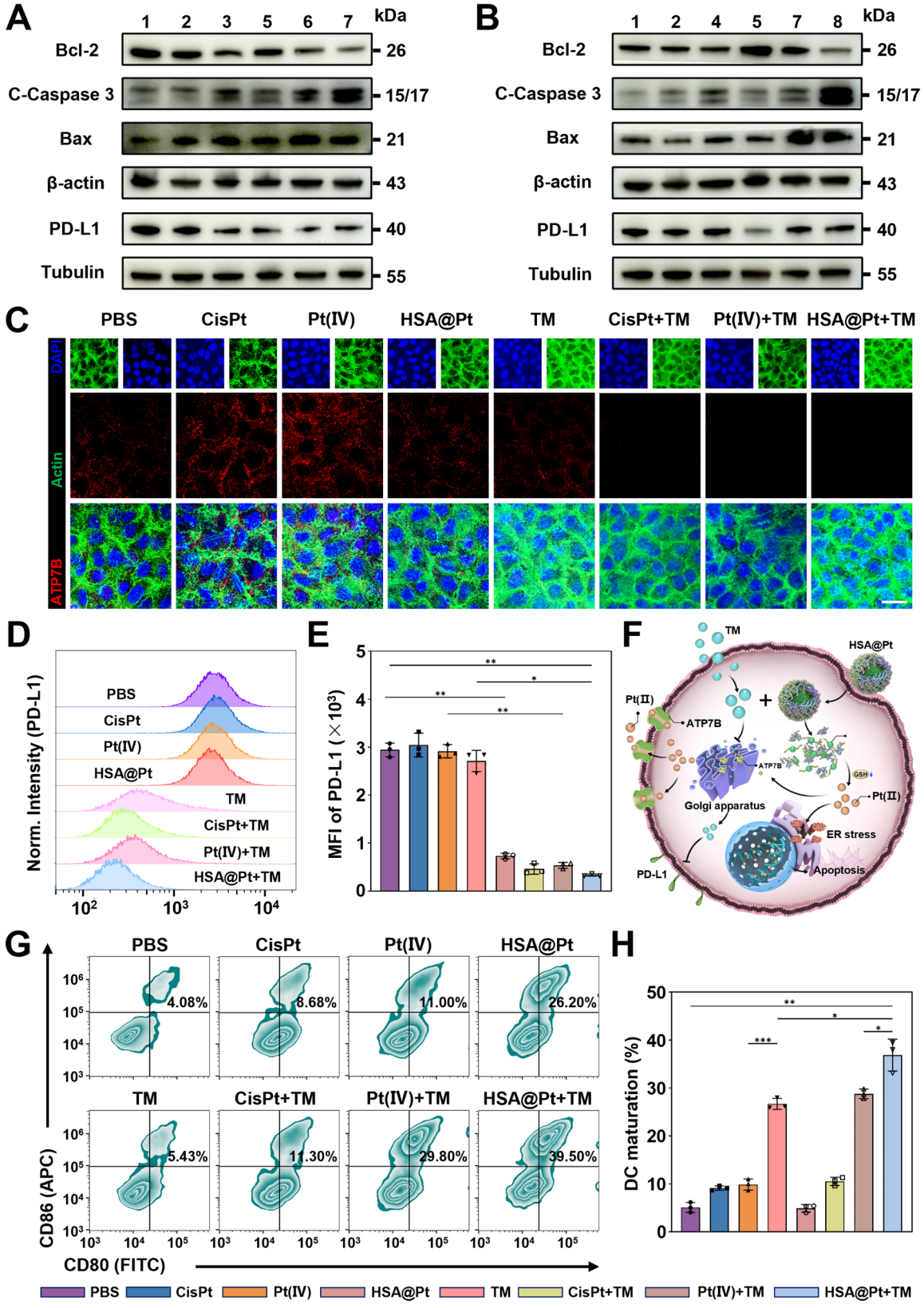

Fig. 4 (See legend on next page.)

(See figure on previous page.)

Fig. 3 Blocked platinum efflux and enhanced ER stress by HSA@Pt combined with TM in vitro. (Aand B) Proteins expression levels of apoptosis-related proteins and PD-L1 in A549 cells after various treatments as mentioned above for 24 h by Western blot. Tubulin and β-actin were used as the internal reference protein. 1: PBS; 2: CisPt; 3: Pt(IV); 4: HSA@Pt; 5:TM; 6: CisPt+TM; 7: Pt(IV)+TM; 8: HSA@Pt+TM; (C) Representative CLSM images to show the ATP7B expression in A549 cells with various treatments. Scalar bar: 50 μm. (D) PD-L1 expression in A549 cells after various treatments by flow cytometry and (E) the corresponding quantification of PD-L1 expression. (F) Schematic illustration of possible mechanism of HSA@Pt combined with TM for antitumor activity. (G) Flow cytometry analysis and (H) quantitative study of DC maturation co-cultured with A549 cells with various treatments. $n = 3$. Data are presented as mean ± SD. Statistical significances between every two groups were calculated *via* one-way ANOVA with Tukey's multiple comparisons test. $^{*}p < 0.05$, $^{**}p < 0.01$, $^{***}p < 0.001$.

downregulating the expression of ATP7B, thereby intensifying the oxidative stress state of the cells.

TM functions as a copper chelator, influencing copper levels and intracellular platinum levels, and thus affecting copper homeostasis. This represents an emerging therapeutic target in oncology. Recent studies have demonstrated that copper ion carriers can induce PD-L1 stabilisation by overloading cancer cells with copper. Furthermore, these studies have shown that copper chelators have the potential to be repurposed for immune checkpoint blockade therapies [27, 28, 40]. In light of these findings, the present study was conducted to analyse the expression levels of PD-L1 protein in A549 cells treated with different drugs by WB. The results demonstrated a notable reduction in PD-L1 expression levels in TM-co-treated cells, when compared to cells treated with the drugs alone (Fig. 3A and S10). Subsequently, to further validate the effect of TM on cellular PD-L1 expression, the study examined the PD-L1 expression levels of A549 cells treated with different drugs separately by flow cytometry. The results demonstrated that, consistent with the WB outcomes, the PD-L1 expression levels of TM co-treated cells exhibited a notable decline. Among the treatments, the PD-L1 expression level of A549 cells treated with HSA@Pt+TM was found to be 8.21 times lower than that of cells treated with HSA@Pt alone (Fig. 3D and E). These findings suggest that TM can regulate copper levels and affect PD-L1 expression in cancer cells.

TM results in the accumulation of platinum drugs in tumor cells, which causes excessive oxidative stress in cells and the release of damage-associated molecular patterns. In the tumor microenvironment, TM-induced down-regulation of PD-L1 may facilitate the recognition of tumor cells by immune cells, impede their immune escape and stimulate antitumor immune responses (Fig. 3F). Finally, in order to test the effect of immune activation of HSA@Pt+TM-treated tumor cells, the study treated A549 cells with different drugs for 24 h, and then co-incubated the tumor cells with mouse bone marrow-derived dendritic cells (BMDCs) for a further 24 h. Flow cytometry was employed to ascertain the maturation of DC cells, and it was determined that HSA@Pt+TM-treated tumor cells were co-incubated with BMDCs, with 36.9% of them exhibiting mature DC cell characteristics (Fig. 3G and H). In conclusion, HSA@Pt+TM-treated tumor cells were observed to release damage-related molecular patterns, thus inducing DC cell maturation and activating antitumor immune effects.

Metabolomic analysis of A549 cells treated with PBS, TM, Cispt and HSA@Pt+TM

Based on the preceding mechanistic investigations, the study validated that the combination of drugs disrupts the redox equilibrium within tumor cells. The relationship between redox homeostasis and metabolism is intricate and interdependent, with both processes contributing to the maintenance of cellular physiological function. In order to gain further insight into the mechanism of action of HSA@Pt+TM in tumor cells, the study employed metabolomic analysis of metabolites in A549 cells with different treatments by liquid chromatography/mass spectrometry (LC-MS). The initial stage of the study involved the application of principal component analysis (PCA) to the quantification of 1,093 metabolites. This analysis revealed that principal components 1 and 2 collectively accounted for 79.3% and 4.9% of all detectable metabolites, respectively. Additionally, the results indicated the absence of outlier samples and the presence of high similarity in intracellular metabolites between the same drug treatments (Figure S11). Subsequently, the study demonstrated the distinctions in intracellular metabolites between disparate drug treatments *via* clustering heatmaps. The results demonstrated that the expression of intracellular metabolites exhibited a similar trend between the HSA@Pt+TM and TM treatments in comparison to the PBS vs. cisplatin treatments. This variability precisely illustrated the differences among the ways in which the different drugs acted (Fig. 4A). The results of the differential metabolite screening were visualised in the form of volcano plots, which also demonstrated the overall distribution of intracellular metabolite differences between drug treatments. The number of intracellular differential metabolites between the HSA@Pt+TM and TM treatments was significantly lower than that observed between the HSA@Pt+TM and other treatments, with only 188 metabolites being up-regulated and 383 down-regulated (Figure S12).

Subsequently, in order to ascertain the mechanism of action of HSA@Pt+TM in regulating tumor cells, the study conducted a KEGG enrichment analysis of differentially expressed metabolites associated with biogenic

energy metabolism, substance transport, signalling, and cell cycle regulation in cells treated with PBS and HSA@Pt+TM. The results demonstrated that metabolites associated with nucleotide metabolism, purine metabolism, the ABC transporter, and the pyrimidine metabolism pathway exhibited notable enrichment in the metabolites of HSA@Pt+TM-treated cells (Fig. 4B). Additionally, the study compared the enrichment analysis of differentially expressed metabolites in cells treated with TM and CisPt. It was observed that the differentially expressed metabolites also exhibited significant enrichment in the ABC transporter pathway in comparison to those of cisplatin-treated cells, further underscoring the role of TM in ATP7B regulation (Figure S13). A comprehensive analysis of the pathways where the differential metabolites were located (including enrichment analysis and topology analysis) was conducted to identify the key pathways with the highest correlation with metabolite differences. The results demonstrated that the differentially expressed metabolites in cells treated with PBS or cisplatin, respectively, and HSA@Pt+TM were also markedly enriched in the purine metabolic pathway (Fig. 4C and S14). Among these pathways, those associated with purine, pyrimidine, and nucleic acid metabolism were linked to the metabolic processes occurring following DNA damage. These findings align with the established mechanism of platinum-induced apoptosis. The study was based on the pre-analysis of differential metabolites obtained from PBS versus HSA@Pt+TM-treated cells to construct a network-based enrichment analysis. The results included metabolic pathways, modules, enzymes, reactions and metabolites, reflecting the intersection between metabolic pathways as well as targeting potential enzymes and metabolites after HSA@Pt+TM-treated cells, thus enhancing the interpretability of the aforementioned mechanism (Fig. 4D).

A metabolic pathway analysis of differentially expressed metabolites revealed that intracellular metabolites involved in the glutamate and glutathione metabolic pathways were also significantly enriched following the PBS vs. HSA@Pt+TM treatment (Fig. 4C). Previous studies have also demonstrated that TM coupled with HSA@Pt has the effect of increasing the intracellular concentration of platinum in tumor cells by down-regulating the expression of ATP7B, thereby further exacerbating the oxidative stress state of the cells. Intracellular oxidative stress represents a pivotal physiological process, characterised by a delicate equilibrium between the generation of reactive oxygen species and the capacity to detoxify and repair the damage incurred as a consequence of these species. Accordingly, the study employed a quantitative approach to compare the metabolites (glutamate, glutathione disulfide, and glutathione) [41] associated with the GSH synthesis pathway in cells following different drug treatments. The levels of GSH synthesis pathway-related metabolites in the metabolites of HSA@Pt+TM-treated cells were found to be significantly lower than those of the corresponding metabolites in the metabolites ofPBS-treated cells, with the former being 1.8-, 6.25-, and 5.56-fold lower, respectively (Fig. 4E-G). In conclusion, the study further corroborated that HSA@Pt+TM could intensify the oxidative stress state of cells and induce apoptosis through metabolomic analysis.

In vivo biodistribution and antitumor effects of HSA@Pt combined with TM

In order to investigate the antitumor effect of HSA@Pt+TM in vivo, the study constructed a subcutaneous lung cancer C57BL/6 mouse model using LLC cells and explored the in vivo distribution of HSA@Pt in mice as well as its antitumor activity in accordance with the relevant administration regimen (Fig. 5A). The favourable biocompatibility, stability and targeting properties of human serum albumin nanomedicines render them a promising option for clinical therapeutic applications [35]. To validate these properties, the study initially monitored the biodistribution of HSA@Pt within living mice. The study employed the IVIS (In Vivo Imaging System for Small Animals) to monitor the fluorescence signals of live mice that had been injected with Cy7.5-labeled HSA@Pt (HSA@Cy7.5) in the tail vein for a period of 48 h. The fluorescence signals of HSA@Pt were quantified in the tail vein of mice that had been injected with Cy7.5-labeled HSA@Pt. It was observed that 1 h after injection, fluorescence could be detected at the tumor site of the mice. Furthermore, the fluorescence intensity at the tumor site demonstrated a continuous increase over time, reaching a peak at approximately 24 h with a value of 3.98×10^9 p/s/cm^2/sr (Fig. 5B and C). The aforementioned findings substantiate the assertion that HSA@Pt is capable of rapidly targeting and accumulating at the tumor site in mice. 24 h following the injection, the mice were euthanised and their major tissue organs and tumor tissues were imaged ex vivo. This revealed that HSA@Cy7.5 was predominantly accumulated in the tumor, liver, and kidney (the major metabolic organs in the body) sites. The average fluorescence value of the tumours reached 1.24×10^7 p/s/cm2/sr (Fig. 5D). In conclusion, the results demonstrated that HSA@Pt was capable of targeting and accumulating in mouse tumor sites, exhibiting a favourable retention effect.

The subsequent phase of the study was to ascertain the in vivo antitumor efficacy of HSA@Pt+TM. Following a 18-day course of treatment with the various drugs, the mice treated with saline and TM exhibited a rapid increase in tumor volume, whereas the mice treated with HSA@Pt and HSA@Pt+TM demonstrated effective tumor inhibition of 50.34% and 63.62%, respectively

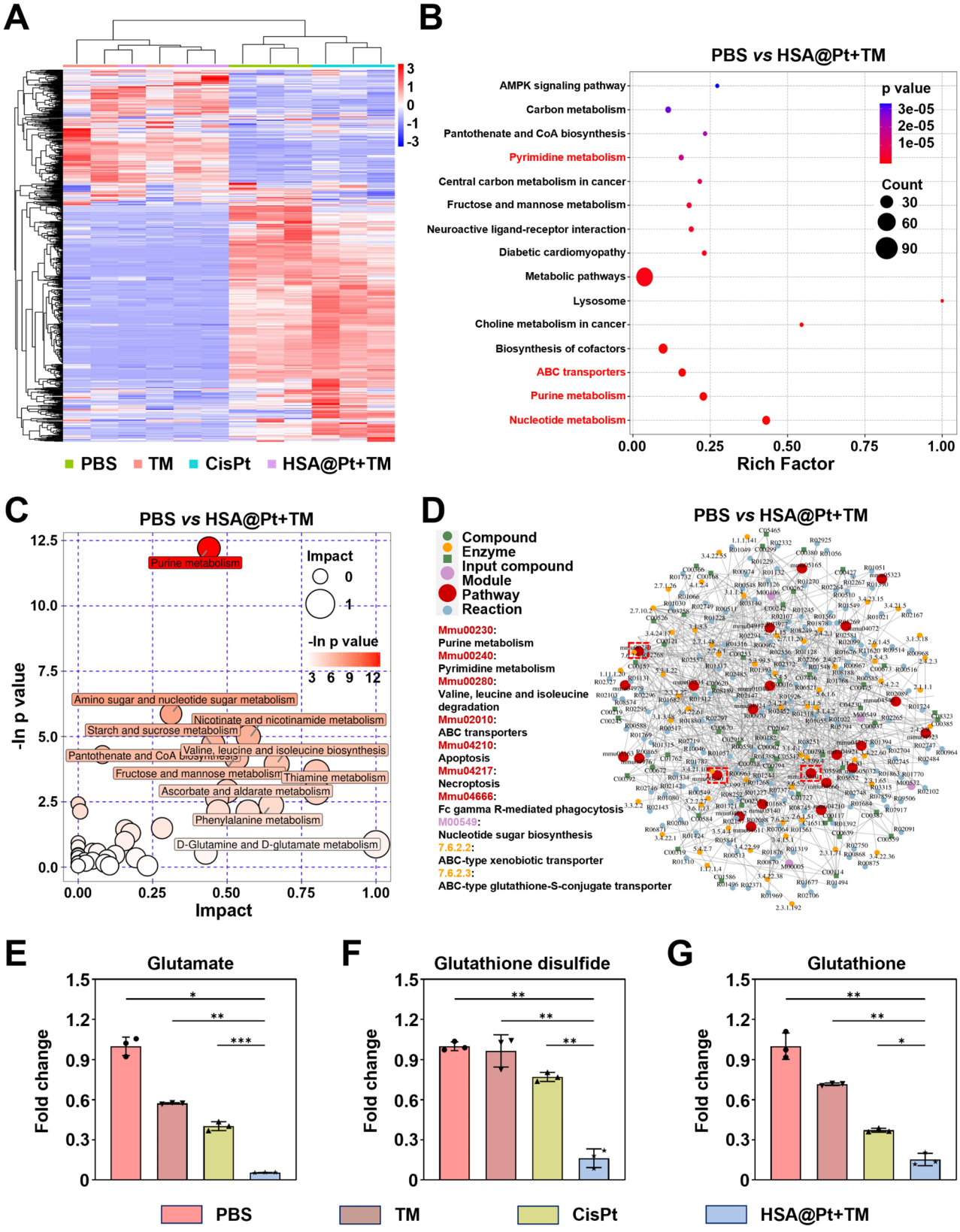

Fig. 5 (See legend on next page.)

(See figure on previous page.)

Fig. 4 Metabolomic analysis of A549 cells treated with PBS, TM, CisPt and HSA@Pt+TM. (A) Heat map showing unsupervised hierarchical clustering of metabolites quantified by liquid chromatography/mass spectrometry. (B) Dot plot depicting the top-15 KEGG enrichment pathways between A549 cells treated with HSA@Pt+TM and PBS. (C) Bubble plot depicting the pathway analysis between A549 cells treated with HSA@Pt+TM and PBS. The size of the dots corresponds to the enrichment ratio, and the color of the dots corresponds to the correlated *p*-value. (D) The network analysis of differentially expressed metabolites between A549 cells treated with HSA@Pt+TM and PBS. Red dots indicate a metabolic pathway, yellow dots represent information on a substance-associated regulatory enzyme, green dots represent a background substance for a metabolic pathway, purple dots represent information on the class of molecular modules of a substance, blue dots represent a substance's chemical interactions, and green squares represent the differences between substances obtained from this comparison. (E-G) Different abundances of associated with GSH metabolism in metabonomic data. $n = 3$. Data are presented as mean ± SD. Statistical significances between every two groups were calculated *via* one-way ANOVA with Tukey's multiple comparisons test. * $p < 0.05$, ** $p < 0.01$, *** $p < 0.001$.

(Fig. 5E). The mean tumor weight in mice treated with HSA@Pt and HSA@Pt + TM was 0.45 g and 0.16 g, respectively, representing a reduction of 1/3 and 1/9 (1.44 g) of the mean tumor weight of control mice (Fig. 5F and H). Subsequently, the long-term survival of the homozygous mice after administration of the drug was observed. The results of the Kaplan-Meier survival analysis demonstrated that, in comparison with the control mice, 5/8 of the HSA@Pt-treated mice perished on the fortieth day, whereas only 3/8 of the HSA@Pt+TM-treated mice did so (Figure S16A). This finding suggests that HSA@Pt+TM significantly improves the long-term survival of mice. The therapeutic efficacy of HSA@Pt+TM was additionally corroborated through the utilisation of H&E (haematoxylin and eosin) and TUNEL (terminal deoxynucleotidyl transferase-mediated dUTP-biotin nick end labelling) staining techniques. Histological examination revealed a marked increase in nuclear fragmentation and nucleolysis in tumor cells of mice treated with HSA@Pt+TM, in comparison to the control group (Fig. 5I (above)). TUNEL staining demonstrated a significantly higher intensity of green fluorescence in the tumor tissues of mice treated with HSA@Pt+TM, indicative of DNA damage in these regions (Fig. 5I (below)). In conclusion, the combination of HSA@Pt and TM demonstrated enhanced antitumor efficacy in a hormonal mouse model.

The safe in vivo application of nanomedicines is contingent upon the fulfilment of two fundamental prerequisites: good biocompatibility and low systemic toxicity. In light of these findings, the study proceeded to assess the in vivo toxicity of HSA@Pt+TM. The study revealed that the body weights of mice treated with CisPt and CisPt+TM exhibited a decrease of 1.48 g and 1.60 g, respectively, which may be attributed to some degree of drug toxicity. In contrast, the body weight of mice treated with HSA@Pt and HSA@Pt + TM exhibited a gradual increase, reaching a range of 16–20 g, which was not statistically different from that of saline-treated mice (Fig. 5G). Subsequently, the study examined the physiological and biochemical indices of the blood of the mice in each group and found no significant difference in the biochemical indices (ALT, AST, ALP, BUN, and CR) between HSA@Pt and HSA@Pt+TM-treated mice when compared to the corresponding biochemical indices in saline-treated mice (Figure S15). Conversely, the blood biochemical parameters were found to be abnormally elevated in mice treated with CisPt and CisPt+TM, indicating the presence of haematological toxicity associated with the drug. Histological examination of the main organs of mice in each group revealed the presence of hemolysis in the liver and kidney of CisPt and CisPt+TM-treated mice, as compared to the control group. In contrast, the cellular morphology of all organs of HSA@Pt and HSA@Pt+TM-treated mice were normal. These findings collectively suggest that the hepatorenal toxicity of CisPt is more pronounced, whereas there is no systemic toxicity in HSA@Pt+TM-treated mice at this dose.

In vivo activation of systemic antitumor immune response by HSA@Pt combined with TM

Prior research has demonstrated that elevated ATP7B protein expression is linked to resistance to chemotherapeutic agents such as cisplatin in tumor cells [42–44]. Conversely, there is an interaction between TM and copper-transporting proteins, which can produce a synergistic effect with cisplatin drugs during cancer chemotherapy [23]. Therefore, the study initially investigated the expression of ATP7B in tumor tissues of mice using immunohistochemistry. The results demonstrated that the expression of ATP7B in tumor tissues was diminished in mice treated with platinum drugs in conjunction with TM in comparison to the single-drug control group (Fig. 6A (above)), thereby substantiating the impact of TM in downregulating ATP7B. The accumulation of platinum in vivo resulted in an exacerbation of oxidative stress within tumor cells, which led to the release of damage-associated molecular patterns (DAMPs). This, in turn, induced antitumor immune responses. Conversely, the copper chelator TM has the potential to be repurposed for immune checkpoint blockade therapy, which could serve to enhance the killing effect of T cells on tumor cells. The study proceeded to examine the expression of PD-L1 in tumor tissues of mice through immunofluorescence. The findings revealed that mice treated with platinum and TM exhibited diminished expression of PD-L1 in their tumor tissues, thereby corroborating the downregulation of PD-L1 by TM (Fig. 6A (middle)).

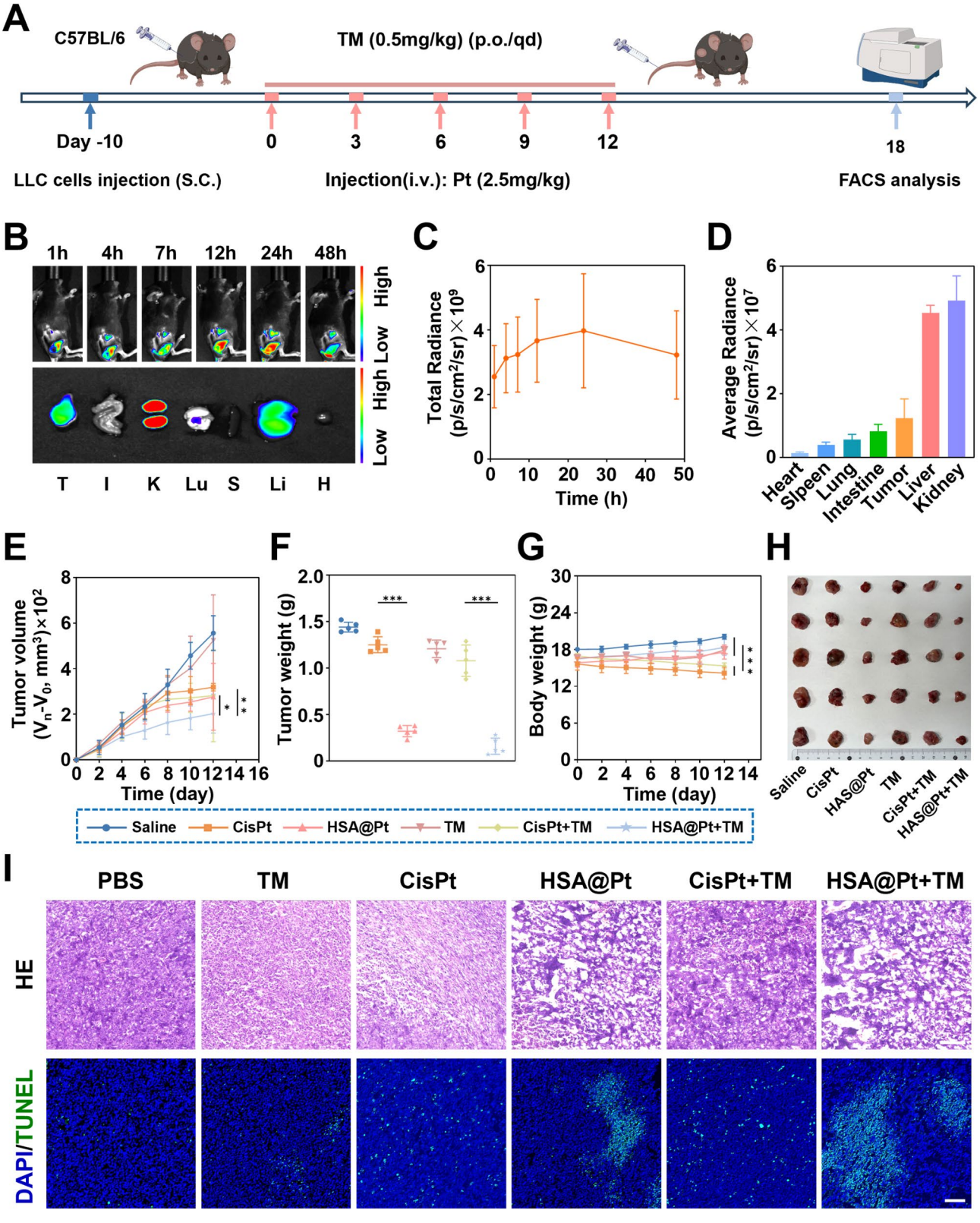

Fig. 6 (See legend on next page.)

(See figure on previous page.)

Fig. 5 In vivo biodistribution and antitumor effects of HSA@Pt combined with TM. (A) Schematic illustration of in vivo treatment and biodistribution study. (B) Tumor imaging of LLC-bearing mice after intravenous injection of HSA@Cy7.5 at different times (top panel). (C) Quantification of fluorescence intensity in mice at different time points and (D) mean fluorescence intensity of HSA@Cy7.5 in major organs and tumor 48 h after intravenous injection. (E) Relative tumor growth inhibition curves and (F) corresponding tumor weight. (G) Body weight changes of mice treated with Saline, CisPt, HSA@Pt, CisPt+TM, HSA@Pt+TM at 2.5 mg Pt/kg or 0.5 mg TM/kg body weight. (H) Representative tumor images of different groups after 18 days of treatment. (I) H&E (above) and TUNEL (below) staining of tumor tissues in various treatments. Scalar bar: 100 μm. $n = 5$. Data are presented as mean ± SD. Statistical significances between every two groups were calculated *via* one-way ANOVA with Tukey's multiple comparisons test. *$p < 0.05$, **$p < 0.01$, ***$p < 0.001$.

In order to gain a deeper understanding of the impact of HSA@Pt+TM treatment on immune system activation in mice, the study examined tumor, spleen and lymphatic tissues from mice treated with different drugs, respectively, and characterised relevant immune indexes by flow cytometry. Firstly, immunofluorescence staining of $CD8^+$ T cells in tumor tissues was conducted. The results demonstrated that, in comparison to the other groups, the mice treated with HSA@Pt+TM exhibited a heightened intensity of CD8 red fluorescence in tumor tissues, indicating that HSA@Pt+TM treatment could enhance the level of $CD8^+$ T cell tumor infiltration (Fig. 6A (below)). Subsequently, the study employed flow cytometry to analyse the maturation of DC cells in tumor and lymphoid tissues of mice treated with different drugs. The results demonstrated that the proportion of mature DC cells ($CD80^+$ $CD86^+$) in lymph nodes of HSA@Pt+TM-treated mice (48.33%) was 5.16 times higher than the proportion of mature DC cells in lymph nodes of control mice (9.37%) (Fig. 6C). Furthermore, the proportion of mature DC cells in tumour tissues of HSA@Pt+TM-treated mice increased by 25.4% compared with the proportion of mature DC cells in tumor tissues of saline-treated mice (Fig. 6F), thereby providing compelling evidence that HSA@Pt+TM treatment can effectively promote DC cell maturation.

Mature DC cells have the capacity to elicit efficacious adaptive immune responses through the activation of T lymphocytes [45]. Subsequently, the relative proportions of $CD4^+$ T cells and $CD8^+$ T cells in the spleen were investigated, and the same was found for the HSA@Pt+TM-treated mice, which exhibited a 1.62-fold increase in the proportion of $CD8^+$ T cells in the spleen (33.87%) compared to that of $CD8^+$ T cells in the spleen of the control mice (20.87%) (Fig. 6B and D), while the proportion of $CD4^+$ T cells rose by 15.30% compared to that of control mice (Fig. 6E). The study then analysed the proportion of $CD4^+$ T cells and $CD8^+$ T cells in the tumor tissues and similarly found that the proportion of $CD4^+$ T cells and $CD8^+$ T cells in the spleen of HSA@Pt+TM treated mice increased by 14.20% and 18.57% respectively compared to the proportion of $CD4^+$ T cells and $CD8^+$ T cells in the tumor tissues of control mice (Fig. 6G and H). Finally, it was also found that HSA@Pt+TM treatment induced the conversion of tumor-associated TAM cells from M2 ($CD80^-$ $CD206^+$) to M1 ($CD80^+$ $CD206^-$) type, with the proportion of M1 TAM cells in the tumor of HSA@Pt+TM-treated mice (22.13%) being approximately 2.95 times higher than that of M1 TAM cells in the tumor of saline-treated mice (7.51%) (Fig. 6I and J). This finding indicates that HSA@Pt+TM has the potential to reverse the immunosuppressive state of TME in mice and synergistically enhance the adaptive immune response. These observations suggest that the combination of HSA@Pt+TM with clinically used immune checkpoint inhibitors (PD1/PD-L1 inhibitors) for immunotherapy-resistant NSCLC patients may become the content and direction of future research.

At 30 days after the first administration of mice, after we executed a batch of mice, we took the spleen tissues of mice, prepared single-cell suspensions, and detected the number of memory T cells in the spleen tissues by flow cytometry. The results demonstrated that the number of central-type memory T cells in the spleen tissues of HSA@Pt+TM-treated mice was approximately 8-fold higher compared to the control mice (Figure S16B and S16C). This finding indicates that HSA@Pt+TM can enhance the persistence of immune memory and the long-term impact of antitumor immunity in mice, and improve the long-term survival of hormonal mice.

Conclusion

To conclude, lung cancer, the most prevalent form of cancer worldwide, has consistently been a primary concern for the medical community and society at large, with a significant focus on its treatment and prevention. Among these, NSCLC has attracted significant attention with regard to its therapeutic applications and related developments. Cisplatin-based adjuvant chemotherapy represents the standard postoperative treatment option for NSCLC. However, the inherent challenges of clinical platinum-based chemotherapy, namely toxicity and drug resistance, limit the effectiveness and clinical application of this approach. In recent years, tetravalent platinum prodrugs have emerged as a pivotal strategy for the development of next-generation platinum drugs. These drugs exhibit enhanced metabolic stability in blood circulation and reduced off-target platinization toxicity compared to traditional platinum drugs. However, it remains ineffective in cisplatin-resistant tumors. A considerable number of studies have concentrated on the functional modification of its moieties and drug-targeted delivery, while the platinum resistance mechanisms generated by the tumor itself have been largely overlooked. Therefore,

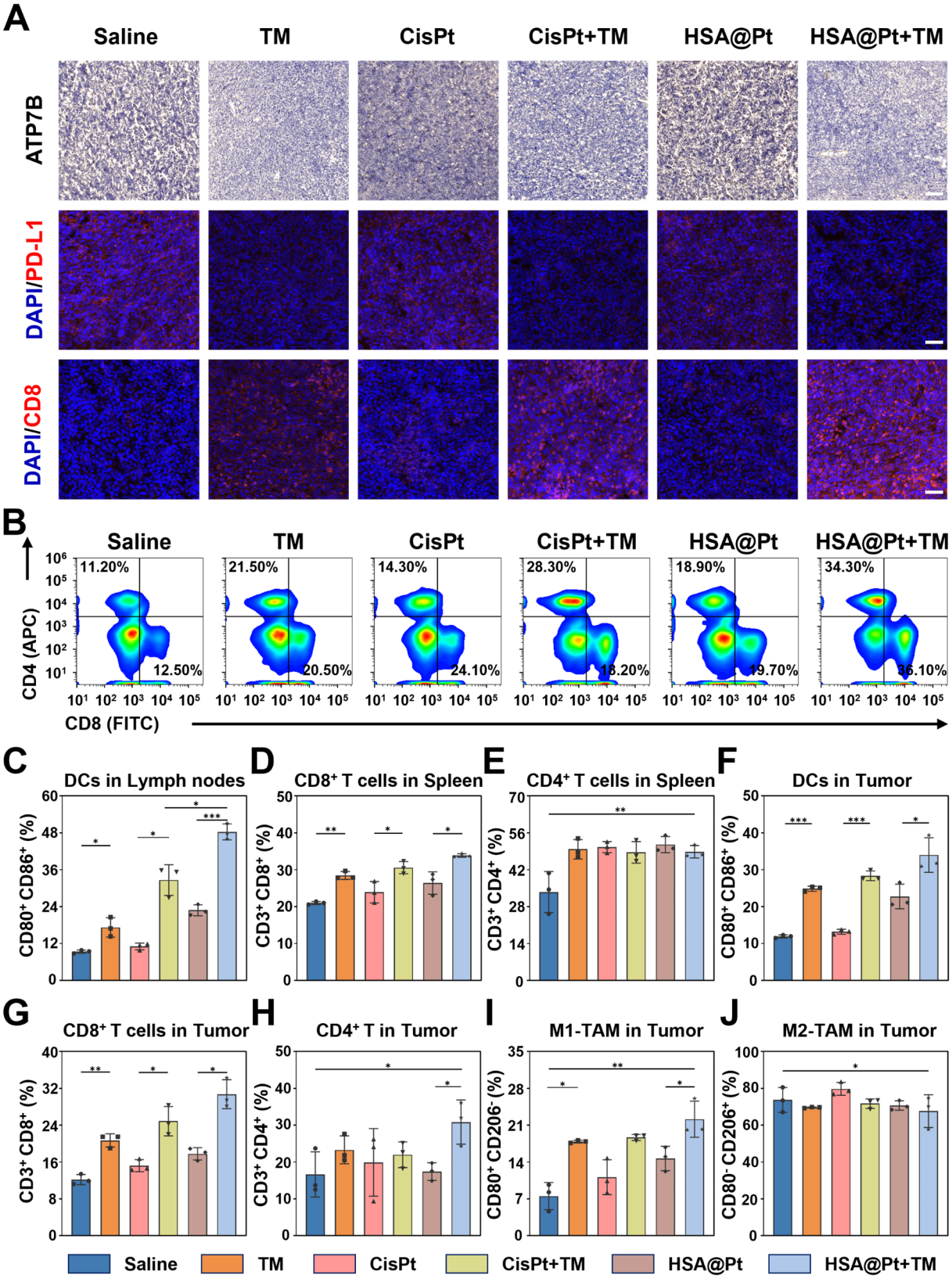

Fig. 7 (See legend on next page.)

(See figure on previous page.)

Fig. 6 In vivo activation of systemic antitumor immune response by HSA@Pt combined with TM. (A) Immunohistochemistry images of ATP7B (above), and immunofluorescence images of PD-L1(middle) and infiltration of CD8+ T cells (below) staining sections within tumor tissues after various treatments. Scale bar: 100 μm. (B) Representative flow cytometric analysis of CD8+ and CD4+ T cells gating on CD3+ cells within spleen after various treatments. (C) The percentages of populations of mature DCs (CD80+ CD86+) within DLNs in each group are presented as histograms. (D) The percentages of populations of CD8+ T cells and (E) CD4+ T cells within spleen in each group are presented as histograms. (F) The percentages of populations of mature DCs (CD80+ CD86+) within tumor in each group are presented as histograms. (G) The percentages of populations of CD8+ T cells and (H) CD4+ T cells within tumor in each group are presented as histograms.(I) The percentages of populations of M1 TAM cells (CD80+ CD206−) and (J) M2 TAM cells (CD80− CD206+) within tumor in each group are presented as histograms. $n = 3$. Data are presented as mean ± SD. Statistical significances between every two groups were calculated *via* one-way ANOVA with Tukey's multiple comparisons test. *$p < 0.05$, **$p < 0.01$, ***$p < 0.001$.

a GSH-responsive albumin nanoparticle (HSA@Pt) was designed and synthesised. The HSA@Pt was found to be highly efficacious and low-toxic, capable of targeted accumulation and retention at the tumor site. Following the co-administration of TM, the release of Pt(IV) from HSA@Pt was facilitated by the depletion of GSH within the tumor microenvironment, resulting in the reduction of Pt(IV) to bivalent platinum and subsequent DNA damage, which ultimately induced cell apoptosis. Meanwhile, TM can enter tumor cells by free diffusion, inhibit the expression of copper transporter proteins ATP7B and PD-L1, and block platinum efflux. These actions synergistically exacerbate the cellular stress state, prompting the cells to release damage-associated molecular patterns and further activate the antitumor immune response. The findings of this study provide experimental evidence that albumin nanoplatinum has the potential to be a clinically applicable drug. Furthermore, they offer a novel approach to the chemo-immunotherapy of clinical NSCLC that involves the repurposing of existing drugs and the use of synergistic sensitisation.

Supplementary Information

The online version contains supplementary material available at https://doi.org/10.1186/s12951-025-03310-4.

Supplementary Information: Supplementary Information to this article contains additional experimental details, Scheme S1 and Figures S1-S22, which is available from authors

Acknowledgements
Not applicable.

Author contributions
The manuscript was written through contributions of all authors. All authors have given approval to the final version of the manuscript.

Funding
This work was supported by the Independent Exploration and Innovation Project for Graduate Students of Central South University (2024ZZTS0286), the Hunan Provincial Graduate Student Research and Innovation Program (CX20240332), the Provincial Natural Science Foundation of China (2023JJ50013), the National Natural Science Foundation of China (82204531, 82073943, 82373962, 82474012), the Scientific research project of Furong Laboratory of Central South University (No.2023SK2083) and the Project of the Guide-driven Original Exploration Program of the National Natural Science Foundation (82450103).

Data availability
No datasets were generated or analysed during the current study.

Declarations

Ethics approval and consent to participate
All animal experiments were conducted in accordance with the guidelines of Hunan SJA Laboratory Institutional Animal Care and Use Committee (SJA2022128).

Consent for publication
Consents for publication were obtained from all the authors of this study.

Competing interests
The authors declare no competing interests.

Received: 18 December 2024 / Accepted: 8 March 2025
Published online: 18 March 2025

References

1. Siegel RL, Giaquinto AN, Jemal A. Cancer statistics, 2024. CA Cancer J Clin. 2024;74:12–49.
2. Han B, Zheng R, Zeng H, Wang S, Sun K, Chen R, Li L, Wei W, He J. Cancer incidence and mortality in China, 2022. J Natl Cancer Cent. 2024;4:47–53.
3. Wu YL, Tsuboi M, He J, John T, Grohe C, Majem M, Goldman JW, Laktionov K, Kim SW, Kato T, et al. Osimertinib in resected EGFR-Mutated Non-Small-Cell lung Cancer. N Engl J Med. 2020;383:1711–23.
4. Zenke Y, Tsuboi M, Chiba Y, Tsujino K, Satouchi M, Sawa K, Shimizu J, Daga H, Fujimoto D, Mori M, et al. Effect of Second-generation vs Third-generation chemotherapy regimens with thoracic radiotherapy on unresectable stage III Non-Small-Cell lung cancer: 10-Year Follow-up of a WJTOG0105 phase 3 randomized clinical trial. JAMA Oncol. 2021;7:904–9.
5. Yang JC, Lee DH, Lee JS, Fan Y, de Marinis F, Iwama E, Inoue T, Rodriguez-Cid J, Zhang L, Yang CT et al. Phase III KEYNOTE-789 study of pemetrexed and platinum with or without pembrolizumab for tyrosine kinase Inhibitor–Resistant, EGFR-Mutant, metastatic nonsquamous Non-Small cell lung Cancer. J Clin Oncol 2024:JCO2302747.
6. Deng Z, Li H, Chen S, Wang N, Liu G, Liu D, Ou W, Xu F, Wang X, Lei D, et al. Near-infrared-activated anticancer platinum(IV) complexes directly photooxidize biomolecules in an oxygen-independent manner. Nat Chem. 2023;15:930–9.
7. Zhou Q, Chen S, Xu Z, Liu G, Zhang S, Wang Z, Tse MK, Yiu SM, Zhu G. Multitargeted Platinum(IV) anticancer complexes bearing pyridinyl ligands as axial leaving groups. Angew Chem Int Ed Engl. 2023;62:e202302156.
8. Wang N, Deng Z, Zhu Q, Zhao J, Xie K, Shi P, Wang Z, Chen X, Wang F, Shi J, Zhu G. An erythrocyte-delivered photoactivatable oxaliplatin nanoprodrug for enhanced antitumor efficacy and immune response. Chem Sci. 2021;12:14353–62.
9. Cao X, Li R, Xiong H, Su J, Guo C, An T, Zong H, Zhao R. Novel Pt(IV) complexes to overcome multidrug resistance in gastric cancer by targeting P-glycoprotein. Eur J Med Chem. 2021;221:113520.
10. Tian HX, Mei J, Cao L, Song J, Rong D, Fang M, Xu Z, Chen J, Tang J, Xiao H, et al. Disruption of Iron homeostasis to induce ferroptosis with Albumin-Encapsulated Pt(IV) nanodrug for the treatment of Non-Small cell lung Cancer. Small. 2023;19:e2206688.
11. Johnstone TC, Suntharalingam K, Lippard SJ. The next generation of platinum drugs: targeted Pt(II) agents, nanoparticle delivery, and Pt(IV) prodrugs. Chem Rev. 2016;116:3436–86.
12. Cao L, Tian H, Fang M, Xu Z, Tang D, Chen J, Yin J, Xiao H, Shang K, Han H, Li X. Activating cGAS-STING pathway with ROS-responsive nanoparticles

delivering a hybrid prodrug for enhanced chemo-immunotherapy. Biomaterials. 2022;290:121856.
13. Mao C, Chen J, Zou T, Zhou Y, Liu J, Li X, Li X, Li M, Pan P, Zhuo W, et al. Genome-wide analysis identify novel germline genetic variations in ADCY1 influencing platinum-based chemotherapy response in non-small cell lung cancer. Acta Pharm Sin B. 2022;12:1514–22.
14. Li YQ, Chen J, Yin JY, Liu ZQ, Li XP. Gene expression and single nucleotide polymorphism of ATP7B are associated with platinum-based chemotherapy response in non-small cell lung cancer patients. J Cancer. 2018;9:3532–9.
15. He J, Wang Z, Wang Y, Zou T, Li XP, Cao L, Chen J. The effects of WISP1 polymorphisms on the prognosis of lung Cancer patients with Platinum-Based chemotherapy. Pharmgenomics Pers Med. 2021;14:1193–203.
16. Yin JY, Meng XG, Qian CY, Li XP, Chen J, Zheng Y, Liu R, Zhou HH, Liu ZQ. Association of positively selected eIF3a polymorphisms with toxicity of platinum-based chemotherapy in NSCLC patients. Acta Pharmacol Sin. 2015;36:375–84.
17. Guo Z, Oradd F, Bagenholm V, Gronberg C, Ma JF, Ott P, Wang Y, Andersson M, Pedersen PA, Wang K, Gourdon P. Diverse roles of the metal binding domains and transport mechanism of copper transporting P-type ATPases. Nat Commun. 2024;15:2690.
18. Wei R, Yang J, Cheng CW, Ho WI, Li N, Hu Y, Hong X, Fu J, Yang B, Liu Y, et al. CRISPR-targeted genome editing of human induced pluripotent stem cell-derived hepatocytes for the treatment of Wilson's disease. JHEP Rep. 2022;4:100389.
19. Tsvetkov P, Coy S, Petrova B, Dreishpoon M, Verma A, Abdusamad M, Rossen J, Joesch-Cohen L, Humeidi R, Spangler RD, et al. Copper induces cell death by targeting lipoylated TCA cycle proteins. Science. 2022;375:1254–61.
20. Li Y, Ma J, Wang R, Luo Y, Zheng S, Wang X. Zinc transporter 1 functions in copper uptake and Cuproptosis. Cell Metab. 2024;36:2118–e21292116.
21. Arnesano F, Natile G. Interference between copper transport systems and platinum drugs. Semin Cancer Biol. 2021;76:173–88.
22. Lukanovic D, Herzog M, Kobal B, Cerne K. The contribution of copper efflux transporters ATP7A and ATP7B to chemoresistance and personalized medicine in ovarian cancer. Biomed Pharmacother. 2020;129:110401.
23. Fang T, Chen W, Sheng Y, Yuan S, Tang Q, Li G, Huang G, Su J, Zhang X, Zang J, Liu Y. Tetrathiomolybdate induces dimerization of the metal-binding domain of ATPase and inhibits platination of the protein. Nat Commun. 2019;10:186.
24. Lasorsa A, Nardella MI, Rosato A, Mirabelli V, Caliandro R, Caliandro R, Natile G, Arnesano F. Mechanistic and structural basis for Inhibition of copper trafficking by platinum anticancer drugs. J Am Chem Soc. 2019;141:12109–20.
25. Huang D, Savage SR, Calinawan AP, Lin C, Zhang B, Wang P, Starr TK, Birrer MJ, Paulovich AG. A highly annotated database of genes associated with platinum resistance in cancer. Oncogene. 2021;40:6395–405.
26. Alvarez HM, Xue Y, Robinson CD, Canalizo-Hernandez MA, Marvin RG, Kelly RA, Mondragon A, Penner-Hahn JE. O'Halloran TV: Tetrathiomolybdate inhibits copper trafficking proteins through metal cluster formation. Science. 2010;327:331–4.
27. Voli F, Valli E, Lerra L, Kimpton K, Saletta F, Giorgi FM, Mercatelli D, Rouaen JRC, Shen S, Murray JE, et al. Intratumoral copper modulates PD-L1 expression and influences tumor immune evasion. Cancer Res. 2020;80:4129–44.
28. Ge EJ, Bush AI, Casini A, Cobine PA, Cross JR, DeNicola GM, Dou QP, Franz KJ, Gohil VM, Gupta S, et al. Connecting copper and cancer: from transition metal signalling to metalloplasia. Nat Rev Cancer. 2022;22:102–13.
29. Ryumon S, Okui T, Kunisada Y, Kishimoto K, Shimo T, Hasegawa K, Ibaragi S, Akiyama K, Thu Ha NT, Monsur Hassan NM, Sasaki A. Ammonium Tetrathiomolybdate enhances the antitumor effect of cisplatin via the suppression of ATPase copper transporting beta in head and neck squamous cell carcinoma. Oncol Rep. 2019;42:2611–21.
30. Jiang AL, Wang M, Liu HM, Liu SM, Song XS, Zou Y, Deng YC, Qin Q, Song YR, Zheng Y. Gasdermin E plasmid DNA/indocyanine green coloaded hybrid nanoparticles with Spatiotemporal controllability to induce pyroptosis for colon cancer treatment. Medcomm-Oncology 2023, 2.
31. Manzari MT, Shamay Y, Kiguchi H, Rosen N, Scaltriti M, Heller DA. Targeted drug delivery strategies for precision medicines. Nat Rev Mater. 2021;6:351–70.
32. Zhang D, Chen Y, Hao M, Xia Y. Putting hybrid nanomaterials to work for biomedical applications. Angew Chem Int Ed Engl. 2024;63:e202319567.
33. Russell P, Esser L, Hagemeyer CE, Voelcker NH. The potential impact of nanomedicine on COVID-19-induced thrombosis. Nat Nanotechnol. 2023;18:11–22.
34. Conde J, Langer R, Rueff J. mRNA therapy at the convergence of genetics and nanomedicine. Nat Nanotechnol. 2023;18:537–40.
35. Lamichhane S, Lee S. Albumin nanoscience: homing nanotechnology enabling targeted drug delivery and therapy. Arch Pharm Res. 2020;43:118–33.
36. Karimi M, Bahrami S, Ravari SB, Zangabad PS, Mirshekari H, Bozorgomid M, Shahreza S, Sori M, Hamblin MR. Albumin nanostructures as advanced drug delivery systems. Expert Opin Drug Deliv. 2016;13:1609–23.
37. Hong S, Choi DW, Kim HN, Park CG, Lee W, Park HH. Protein-Based nanoparticles as drug delivery systems. Pharmaceutics 2020, 12.
38. Tang C, Livingston MJ, Safirstein R, Dong Z. Cisplatin nephrotoxicity: new insights and therapeutic implications. Nat Rev Nephrol. 2023;19:53–72.
39. Yuan J, Ofengeim D. A guide to cell death pathways. Nat Rev Mol Cell Biol. 2024;25:379–95.
40. Huang Y, Liu X, Zhu J, Chen Z, Yu L, Huang X, Dong C, Li J, Zhou H, Yang Y, Tan W. Enzyme core spherical nucleic acid that enables enhanced Cuproptosis and antitumor immune response through alleviating tumor hypoxia. J Am Chem Soc. 2024;146:13805–16.
41. Guo W, Li K, Sun B, Xu D, Tong L, Yin H, Liao Y, Song H, Wang T, Jing B, et al. Dysregulated glutamate transporter SLC1A1 propels cystine uptake via Xc(-) for glutathione synthesis in lung Cancer. Cancer Res. 2021;81:552–66.
42. Yu Z, Cao W, Ren Y, Zhang Q, Liu J. ATPase copper transporter A, negatively regulated by miR-148a-3p, contributes to cisplatin resistance in breast cancer cells. Clin Transl Med. 2020;10:57–73.
43. da Costa A, Baiocchi G. Genomic profiling of platinum-resistant ovarian cancer: the road into druggable targets. Semin Cancer Biol. 2021;77:29–41.
44. Lahtinen A, Lavikka K, Virtanen A, Li Y, Jamalzadeh S, Skorda A, Lauridsen AR, Zhang K, Marchi G, Isoviita VM, et al. Evolutionary States and trajectories characterized by distinct pathways stratify patients with ovarian high grade serous carcinoma. Cancer Cell. 2023;41:1103–e11171112.
45. Li QJ, Wu P, Du QJ, Hanif U, Hu HB, Li K. cGAS-STING, an important signaling pathway in diseases and their therapy. Medcomm 2024, 5.

Publisher's note

Springer Nature remains neutral with regard to jurisdictional claims in published maps and institutional affiliations.